Driving mechanism and dynamic fluctuations of charge density waves in the kagome metal ScV$_6$Sn$_6$

Shuyuan Liu,[1,2] Chongze Wang,[1,2,*] Shichang Yao,[2] Yu Jia,[1,3,4] Zhenyu Zhang,[5,†] and Jun-Hyung Cho [1,2,‡]

[1]*Joint Center for Theoretical Physics, School of Physics and Electronics, Henan University, Kaifeng 475004, People's Republic of China*
[2]*Department of Physics and Research Institute for Natural Science, Hanyang University, 222 Wangsimni-ro,*
Seongdong-Ku, Seoul 04763, Republic of Korea
[3]*Key Laboratory for Special Functional Materials of the Ministry of Education, Henan University,*
Kaifeng 475004, People's Republic of China
[4]*Institute of Quantum Materials and Physics, Henan Academy of Sciences, Zhengzhou 450046, China*
[5]*International Center for Quantum Design of Functional Materials (ICQD), and Hefei National Laboratory,*
University of Science and Technology of China, Hefei 230026, China

In contrast to the AV$_3$Sb$_5$ (A = K, Rb, Cs) family exhibiting the ubiquitous $2 \times 2 \times 2$ charge density wave (CDW) order, only ScV$_6$Sn$_6$ in the RV$_6$Sn$_6$ (R = Sc, Y, La) family displays the unusual CDW with a $\sqrt{3} \times \sqrt{3}$ in-plane ordering and a tripling of the unit cell along the c axis. Here, using first-principles density-functional theory calculations, we show that both the $\sqrt{3} \times \sqrt{3} \times 2$ and $\sqrt{3} \times \sqrt{3} \times 3$ CDW orderings can be driven by a Jahn-Teller-like effect where the Sn atoms residing in the kagome bilayers partially undergo delicately different schemes of interlayer dimerization, accompanied by charge redistribution between such Sn atoms and band-gap opening. Counterintuitively, whereas the $\sqrt{3} \times \sqrt{3} \times 2$ phase is energetically more stable than $\sqrt{3} \times \sqrt{3} \times 3$, the latter is thermodynamically stabilized above the CDW transition temperature T_{CDW} by its higher configurational entropy contributed by degenerate fluctuating phases, and is kinetically selected below T_{CDW}, as corroborated by experimental observation of the accompanying first-order phase transition. Our findings reveal the order-disorder nature of the $\sqrt{3} \times \sqrt{3} \times 3$ CDW phase transition in ScV$_6$Sn$_6$, with broader implications for understanding charge orderings and CDW fluctuations in other kagome metals.

Introduction. The two-dimensional (2D) kagome lattice consisting of corner-sharing triangles has attracted tremendous attention due to its unique electronic structure involving a flat band, Dirac cone, and van Hove singularities (VHSs) [1–3]. So far, many experimental and theoretical works in different kagome compounds have presented a wide variety of novel quantum phenomena like anomalous Hall effect [4–6], spin liquid [7,8], flatband ferromagnetism [9], charge density wave (CDW) [10,11], and superconductivity [12–14]. Specifically, a family of V-based kagome metals AV$_3$Sb$_5$ (A = K, Rb, Cs) possesses nontrivial band topology and correlated many-body states such as the unconventional CDW order breaking both time-reversal and rotational symmetries [15,16], electronic nematicity [17,18], and superconductivity [19–22]. Considering that the AV$_3$Sb$_5$ compounds have the saddle points of linearly dispersive Dirac bands at three inequivalent M points near the Fermi level E_F, the nesting of such VHSs was proposed to be a driving mechanism for the CDW formation via electron-electron interaction [23–26]. However, the origin of CDW in AV$_3$Sb$_5$ is still under debate, together with momentum-dependent electron-phonon coupling or phonon softening [27–31]. To resolve this debate,

more extensive studies of the CDW formation in other V-based kagome metals are highly desired.

Recently, among the new nonmagnetic RV$_6$Sn$_6$ (R = Sc, Y, La) family consisting of V kagome bilayers [see Fig. 1(a)], only ScV$_6$Sn$_6$ undergoes a first-order CDW transition at $T_{CDW} \approx 92$ K [32]. Here, ScV$_6$Sn$_6$ was experimentally observed to exhibit a $\sqrt{3} \times \sqrt{3} \times 3$ CDW order, which is distinct from the $2 \times 2 \times 2$ CDW order in AV$_3$Sb$_5$ [10,33]. Such entirely different wave lengths and orientations of the CDW orders between ScV$_6$Sn$_6$ and AV$_3$Sb$_5$ may provide a new route to gain insights into the origin of the CDW order in V-based kagome metals. Specifically, while the CDW order in AV$_3$Sb$_5$ accompanies large in-plane displacements of the V atoms [33], that in ScV$_6$Sn$_6$ is dominated by displacements of the Sc and Sn atoms along the c axis [34]. These unusual features of the CDW order in ScV$_6$Sn$_6$ challenge the nesting scenario because the scattering between the M saddle points near E_F cannot be responsible for a driving force of the $\sqrt{3} \times \sqrt{3} \times 3$ periodic lattice distortion.

For ScV$_6$Sn$_6$, diffuse scattering (DS) and inelastic x-ray scattering (IXS) experiments [35] reported the presence of an order-disorder CDW phase transition at T_{CDW}, where the disordered phase containing a short-range $\sqrt{3} \times \sqrt{3} \times 2$ CDW order was suppressed and replaced by a long-range $\sqrt{3} \times \sqrt{3} \times 3$ CDW order. Another DS and IXS experiment [36] observed that the low-energy longitudinal phonon with propagation wavevector $q^* = (\frac{1}{3}, \frac{1}{3}, \frac{1}{2})$ collapses at ~98 K due to the electron-phonon interaction. Here, the collapse of a

*Corresponding author: cho@henu.edu.cn
†Corresponding author: zhangzy@ustc.edu.cn
‡Corresponding author: chojh@hanyang.ac.kr

soft mode at q^* is driven by a softening of a flat phonon plane at $k_z = \pi$, characterized by an out-of-plane vibration of the trigonal Sn atoms. However, the long-range charge order does not emerge at q^* but at a different wavevector $q_s = (\frac{1}{3}, \frac{1}{3}, \frac{1}{3})$. It is interesting to compare the characteristics of order-disorder CDW phase transition between ScV_6Sn_6 and AV_3Sb_5. For AV_3Sb_5, recent DS and IXS experiments [37–39] also reported a first-order CDW phase transition that features an order-disorder transformation type with strong CDW fluctuations above T_{CDW}. Note that inelastic x-ray, neutron, and Raman scattering experiments for AV_3Sb_5 [37–39] have observed the absence of the lattice collapse at T_{CDW}. Therefore, both ScV_6Sn_6 [35,40] and AV_3Sb_5 [37–39] undergo the first-order, order-disorder CDW phase transition, but their characteristics are apparently distinct from each other: i.e., ScV_6Sn_6 features a first-order transition with phonon softening while AV_3Sb_5 exhibits CDW fluctuations with the absence of phonon softening. Specifically, the temperature evolution of the integrated IXS intensities in ScV_6Sn_6 [35] showed that the maximum peak intensity of the $\sqrt{3} \times \sqrt{3} \times 3$ CDW order below T_{CDW} is at least 3 orders of magnitude larger than that of the short-range $\sqrt{3} \times \sqrt{3} \times 2$ CDW order above T_{CDW}. This huge different IXS intensities of two CDW orders together with the inconsistency between the soft q^*-phonon and q_s-CDW wavevectors are puzzling. Microscopic understanding of such an unconventional CDW phase transition in ScV_6Sn_6 is yet to be identified.

In this Letter, we investigate the driving mechanism of CDW and the nature of CDW phase transition in ScV_6Sn_6 using first-principles density-functional theory (DFT) calculations. We demonstrate that both the $\sqrt{3} \times \sqrt{3} \times 2$ and $\sqrt{3} \times \sqrt{3} \times 3$ CDW orderings can be driven by a Jahn-Teller-like effect where the Sn atoms residing in kagome bilayers are partially dimerized along the c axis together with the charge redistribution between such Sn atoms and its associated band-gap opening. The $\sqrt{3} \times \sqrt{3} \times 3$ phase is found to be energetically less stable than $\sqrt{3} \times \sqrt{3} \times 2$, but the former becomes thermodynamically stabilized above T_{CDW} due to its higher vibrational, electronic, and configurational entropies compared to the latter. Furthermore, we reveal that, while the $\sqrt{3} \times \sqrt{3} \times 3$ CDW order shows dynamic fluctuations between its degenerate configurations above T_{CDW}, it is kinetically trapped below T_{CDW}, thereby leading to the first-order, order-disorder phase transition with a release of configurational entropy at T_{CDW}. Therefore, we conclude that the majority of disordered phase above T_{CDW} is composed of the dynamically fluctuating $\sqrt{3} \times \sqrt{3} \times 3$ CDW order, while the minority is a local ordering of the short-range $\sqrt{3} \times \sqrt{3} \times 2$ CDW order due to a relatively higher energy barrier between its degenerate configurations, as discussed below.

Results. We begin by optimizing the atomic structure of the $1 \times 1 \times 1$ pristine phase of ScV_6Sn_6 using the DFT scheme [41]. Figure 1(a) shows the optimized structure of the pristine phase with the symmetry of space group $P6/mmm$, which is composed of the two V_3Sn1 kagome layers with the triangular Sn1 sublattice centered on the V hexagons of each kagome lattice and the Sn2 honeycomb or Sn3/Sc honeycomb/triangular layer between neighboring V_3Sn1 kagome layers. The electronic band structure of this pristine phase is displayed in
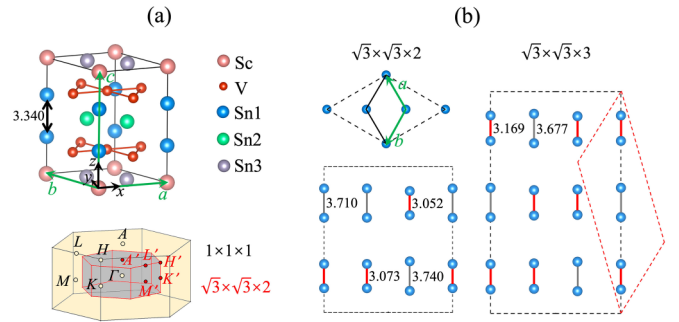

FIG. 1. Atomic structure of pristine and CDW phases of ScV_6Sn_6. (a) Optimized structure of the $1 \times 1 \times 1$ pristine phase of ScV_6Sn_6, together with its Brillouin zone. The top/side views of Sn dimers in the $\sqrt{3} \times \sqrt{3} \times 2$ and $\sqrt{3} \times \sqrt{3} \times 3$ phases are drawn in (b). The black dashed lines in (b) represent the hexagonal unit cells, while the red dashed line in the $\sqrt{3} \times \sqrt{3} \times 3$ phase represents its primitive rhombohedral unit cell. The numbers represent the Sn1-Sn1 bond lengths in angstroms.

Fig. 2(a), together with its projection onto the V $3d$ and Sn $5p$ orbitals (see also Fig. S1 in the Supplemental Material [51]). We find that the bands with momentum-dependent orbital characters near E_F agree well with angle-resolved photoemission spectroscopy (ARPES) and optical reflection measurements [52–54]: i.e., the states along the Γ-M-K-Γ line originate from all the five V d orbitals, while those along the A-L-H-A line mainly originate from the Sn1 p_z and V $d_{xz,yz}$ orbitals. The latter hybridized states in the V_3Sn1
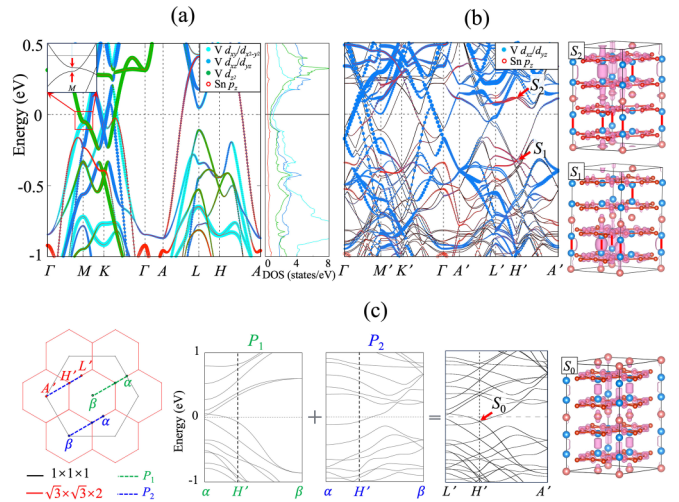

FIG. 2. Electronic structure of pristine and CDW phases of ScV_6Sn_6. Calculated band structures of the (a) pristine and (b) $\sqrt{3} \times \sqrt{3} \times 2$ phases of ScV_6Sn_6. The bands are projected onto V $3d$ and Sn $5p$ orbitals, where the radii of circles are proportional to the weights of the corresponding orbitals. In (a), the PDOS and two saddle points at the M point (indicated by arrows in the inset) are included. In (b), the charge characters of the S_1 and S_2 states at the H' point are displayed with an isosurface of $8 \times 10^{-3} e/Å^3$. In (c), the pristine bands along the three α-β paths (one P_1 and two P_2) are folded to form the sixfold degenerate state S_0 at H', the charge character of which is also displayed with an isosurface of $8 \times 10^{-3} e/Å^3$.

kagome layers play a crucial role in the CDW formation, as discussed below. Meanwhile, two saddle points at the M point close to E_F (indicated by red arrows) don't produce the corresponding VHSs in the partial density of states (PDOS) [see Fig. 2(a)]. Therefore, we can say that the Fermi-surface nesting of saddle-point-derived VHSs between three distinct M points [55], previously proposed in AV_3Sb_5 [23–26], is not responsible for the driving mechanism of the CDW order in ScV_6Sn_6 [34]. Indeed, the electronic states along the Γ-M-K-Γ line remain intact across the CDW transition, as will be shown later.

To explore the phonon instability of the pristine structure of ScV_6Sn_6, we calculate its phonon spectrum using the frozen-phonon method [47,48]. As shown in Fig. S4(a) [51], there exist imaginary phonon modes along the entire A-L-H-A line, the lowest one of which is located at the $H = (\frac{1}{3}, \frac{1}{3}, \frac{1}{2})$ point, leading to a structural reconstruction within the $\sqrt{3} \times \sqrt{3} \times 2$ unit cell. Here, the H-phonon mode represents the Sn1-Sn1 bond-stretching vibrations along the c axis (see Fig. S4(b) [51]). The resulting $\sqrt{3} \times \sqrt{3} \times 2$ CDW order with the D_{6h} symmetry of space group $P6/mmm$ becomes more stable than the pristine phase by 12.59 meV per formula unit (f.u.). In the $\sqrt{3} \times \sqrt{3} \times 2$ CDW structure, the Sn1-Sn1 bond length d_{dimer} [see Fig. 1(b)] is shortened (lengthened) to be 3.052 or 3.073 Å (3.710 or 3.740 Å) compared to that (3.339 Å) in the pristine structure. Hereafter, two Sn1 atoms between neighboring V_3Sn1 kagome layers are termed Sn dimers. While the CDW structure of AV_3Sb_5 has the large in-plane displacement of V kagome sublattice forming trimers and hexamers [33], that of ScV_6Sn_6 has the minimal displacement of V atoms with the large out-of-plane displacement of Sc and Sn atoms [34]. The variations of d_{dimer} during the CDW formation of ScV_6Sn_6 implies a charge transfer from the longer to the shorter Sn dimers, which in turn opens partial CDW gaps around the $H' = (\frac{1}{3}, 0, \frac{1}{4})$ point [see Fig. 2(b)]. Note that (i) the folded pristine band structure onto the $\sqrt{3} \times \sqrt{3} \times 2$ supercell shows that the hybridized Sn1 p_z and V $d_{xz,yz}$ states [S_0 in Fig. 2(c)] at H' on the boundary of Brillouin zone have the sixfold degeneracy, which is split into the three occupied and three unoccupied states in the $\sqrt{3} \times \sqrt{3} \times 2$ phase [see Fig. 2(b)] and (ii) the unfolded band structure of the $\sqrt{3} \times \sqrt{3} \times 2$ phase shows little change along the Γ-M-K-Γ line around E_F (see Fig. S5 [51]). Here, the sixfold degeneracy at H' is generated by the folding of pristine bands along three different paths [see Fig. 2(c)]. As shown in Figs. 2(b) and 2(c), the charge character of the highest (lowest) occupied S_1 (unoccupied S_2) state at H' represents the charge accumulation (depletion) in the shorter (longer) Sn1-Sn1 bonds, compared to the S_0 state in the pristine phase. Therefore, the $\sqrt{3} \times \sqrt{3} \times 2$ CDW order can be attributed to a Jahn-Teller-like effect involving the Sn1-Sn1 bond distortions, the charge redistribution between such Sn dimers, and the resultant partial gap opening around the H' point.

Table I shows the comparison of the lattice constants and d_{dimer} in the pristine phase of RV_6Sn_6 (R = Sc, Y, La). We find that the lattice constants $a = b$ and c in YV_6Sn_6 (LaV_6Sn_6) are larger than those in ScV_6Sn_6 by 0.84(1.91)% and 0.14(0.63)%, respectively. Meanwhile, YV_6Sn_6 (LaV_6Sn_6) has a much shorter d_{dimer} value of 3.151(3.051) Å, compared

TABLE I. Calculated lattice constants and d_{dimer} in the pristine phase of RV_6Sn_6 (R = Sc, Y, La).

	$a = b$ (Å)	c (Å)	d_{dimer} (Å)
ScV_6Sn_6	5.453	9.235	3.339
YV_6Sn_6	5.499	9.248	3.151
LaV_6Sn_6	5.557	9.293	3.051

to that (3.339 Å) in ScV_6Sn_6. Note that the d_{dimer} values in the former compounds are close to the shortest one (3.052 Å) in the $\sqrt{3} \times \sqrt{3} \times 2$ CDW phase of ScV_6Sn_6. Therefore, we can say that the Jahn-Teller-like CDW formation with the Sn1-Sn1 bond distortions and their charge redistribution would not be necessary in YV_6Sn_6 and LaV_6Sn_6. According to the magnetization and x-ray diffraction measurements [56] of Y- and Lu-doped ScV_6Sn_6 where Sc is substituted by larger Y or Lu, the CDW order was observed to be suppressed because the Sn1-Sn1 bond length is reduced by Y and Lu doping. It is thus expected that external perturbations such as chemical doping and pressure in RV_6Sn_6 can tune the Sn1-Sn1 bond length to suppress or create CDW orders.

Unlike the DFT prediction of the $\sqrt{3} \times \sqrt{3} \times 2$ CDW ground state [34], experimental evidence [32,36,57] showed that ScV_6Sn_6 undergoes a CDW transition to the $\sqrt{3} \times \sqrt{3} \times 3$ phase at $T_{\mathrm{CDW}} \approx 92$ K. Therefore, the temperature versus free-energy landscape for the $\sqrt{3} \times \sqrt{3} \times 2$ and $\sqrt{3} \times \sqrt{3} \times 3$ phases can be illustrated like Fig. 3(a): i.e., the free energy of the $\sqrt{3} \times \sqrt{3} \times 3$ phase becomes lower than that of the $\sqrt{3} \times \sqrt{3} \times 2$ phase above T_{CDW}. Our DFT calculations show that at zero temperature, the total energy of the $\sqrt{3} \times \sqrt{3} \times 3$
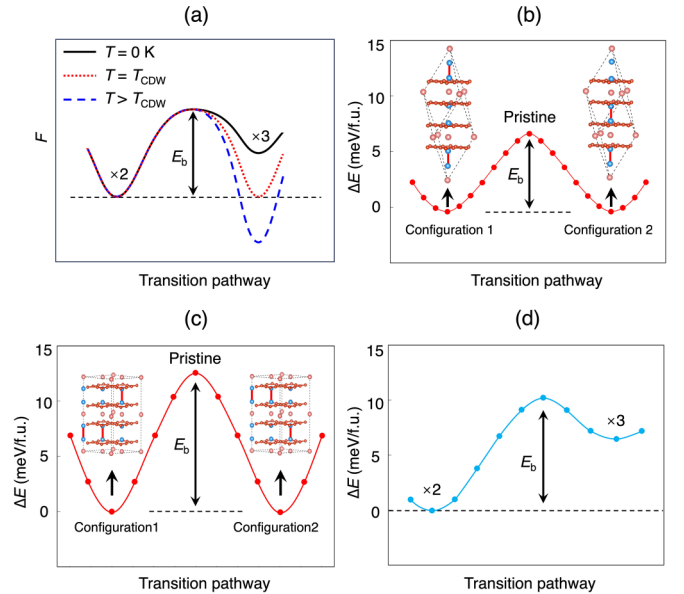

FIG. 3. (a) Schematic free-energy landscape of the $\sqrt{3} \times \sqrt{3} \times 2$ and $\sqrt{3} \times \sqrt{3} \times 3$ phases at different temperatures and the energy profiles along the transition pathways (b) between degenerate $\sqrt{3} \times \sqrt{3} \times 3$ configurations, (c) between degenerate $\sqrt{3} \times \sqrt{3} \times 2$ configurations, and (d) between the $\sqrt{3} \times \sqrt{3} \times 2$ and $\sqrt{3} \times \sqrt{3} \times 3$ phases. The E_b values in (b), (c), and (d) are estimated as 6.30, 12.59, and 10.24 meV/f.u., respectively.
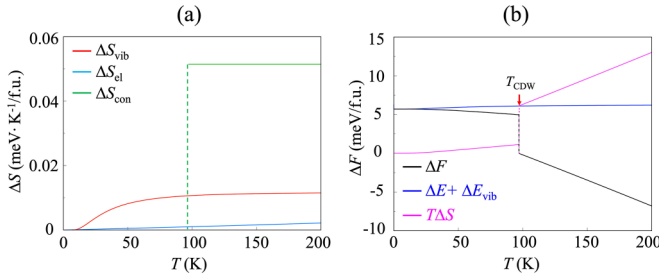
FIG. 4. Calculated ΔS and ΔF. (a) ΔS_{vib}, ΔS_{el}, ΔS_{con}, and (b) ΔF as a function of T. In (b), the calculated values of $\Delta E + \Delta E_{vib}$ and $T\Delta S$ are also included.

phase is higher than that of the $\sqrt{3} \times \sqrt{3} \times 2$ phase by $\Delta E = 6.29$ meV/f.u. The $\sqrt{3} \times \sqrt{3} \times 3$ CDW structure has two different kinds of the Sn1-Sn1 bonds with $d_{dimer} = 3.169$ and 3.677 Å [see Fig. 1(b)]. Meanwhile, the band structure of the $\sqrt{3} \times \sqrt{3} \times 3$ phase is overall the same as that of the $\sqrt{3} \times \sqrt{3} \times 2$ phase (see Fig. S5 [51]), but the former has a CDW gap of 309 meV at the $H'' = (\frac{1}{3}, 0, \frac{1}{3})$ point, slightly smaller than that (440 meV at H') in the latter.

To estimate T_{CDW}, we calculate the Helmholtz free-energy difference $\Delta F = \Delta E + \Delta E_{vib} - T\Delta S$ between the $\sqrt{3} \times \sqrt{3} \times 3$ and $\sqrt{3} \times \sqrt{3} \times 2$ phases where E_{vib} represents vibrational energy [58] and S includes three different types of entropy such as vibrational entropy S_{vib}, electronic entropy S_{el}, and configurational entropy S_{con}. S_{vib} is calculated from the phononic DOS $g^{ph}(\epsilon)$ [47,48]:

$$S_{vib} = -3k_B \int g^{ph}(\epsilon)(n(\epsilon)\ln[n(\epsilon)]$$
$$- [1 + n(\epsilon)]\ln[1 + n(\epsilon)])d\epsilon, \quad (1)$$

where k_B is the Boltzmann constant and $n(\epsilon)$ is the Bose-Einstein population of a state of energy ϵ at T. Figure 4(a) displays $\Delta S_{vib} = S_{vib,\sqrt{3}\times\sqrt{3}\times3} - S_{vib,\sqrt{3}\times\sqrt{3}\times2}$ as a function of T, indicating that the $\sqrt{3} \times \sqrt{3} \times 3$ phase has larger S_{vib} than the $\sqrt{3} \times \sqrt{3} \times 2$ phase. Therefore, $T\Delta S_{vib}$ increases with increasing T (see Fig. S6 [51]), leading to a decrease in ΔF. Next, we calculate S_{el} from the electronic DOS $g^{el}(\epsilon)$:

$$S_{el} = -k_B \int g^{el}(\epsilon)(n(\epsilon)\ln[n(\epsilon)]$$
$$+ [1 - n(\epsilon)]\ln[1 - n(\epsilon)])d\epsilon, \quad (2)$$

where $n(\epsilon)$ is the Fermi-Dirac distribution function. Since the $\sqrt{3} \times \sqrt{3} \times 3$ phase has higher $g^{el}(E_F)$ than the $\sqrt{3} \times \sqrt{3} \times 2$ phase (see Fig. S7 [51]), the former has larger S_{el} than the latter. However, due to the much smaller values of S_{el} [see Fig. 4(a)], $T\Delta S_{el}$ plays a minor role in lowering ΔF. Finally, we consider S_{con} arising from the number of degenerate configurations to which the system can be accessible. Using the nudged elastic band method [49,50], we obtain an energy barrier $E_b = 6.30$ meV/f.u. along the transition pathway TP$_1$ between degenerate configurations in the $\sqrt{3} \times \sqrt{3} \times 3$ structure [see Fig. 3(b)], leading to strong CDW fluctuations above T_{CDW}, as discussed below. Consequently, the $\sqrt{3} \times \sqrt{3} \times 3$ phase can attain a configuration entropy of $S_{con} = k_B\ln(6)/3 = 0.051$ meV K^{-1}/f.u. above T_{CDW} because there are six degen-

erate configurations within the primitive unit cell containing three formula units (see Fig. S8 [51]). On the other hand, the $\sqrt{3} \times \sqrt{3} \times 2$ phase has relatively higher values of energy barrier [see Fig. 3(c)] and free energy [see Fig. 3(a)] above T_{CDW} compared to the $\sqrt{3} \times \sqrt{3} \times 3$ phase, leading to $S_{con} = 0$ without dynamic fluctuations between degenerate configurations. Note that DS and IXS experiments [35,40] observed the $\sqrt{3} \times \sqrt{3} \times 2$ phase above T_{CDW} as a local short-range ordering. Given the estimated values of ΔE, ΔE_{vib}, $T\Delta S_{vib}$, $T\Delta S_{el}$, $T\Delta S_{con}$, we find that the F of the high-entropy $\sqrt{3} \times \sqrt{3} \times 3$ phase becomes equal to that of the $\sqrt{3} \times \sqrt{3} \times 2$ phase at ~ 97 K, where $T\Delta S_{vib} = 1.03$ meV/f.u., $T\Delta S_{el} = 0.10$ meV/f.u., $T\Delta S_{con} = 4.99$ meV/f.u., and $\Delta E_{vib} = -0.17$ meV/f.u. [58] are obtained. This predicted T_{CDW} value is close to the experimental value of ~ 92 K [32] [see Fig. 4(b)], with highlighting the dominant role of configurational entropy in the $\sqrt{3} \times \sqrt{3} \times 3$ CDW formation.

According to the Arrhenius equation [59], the transition rate R can be estimated as $R = \nu \exp(-\frac{E_b}{k_B T})$, where ν is the attempt frequency and E_b is the activation barrier. To estimate R along TP$_1$, we adopt ν with the frequency (~ 1.4 THz) of the Sn1-Sn1 bond-stretching phonon modes around the H point in the $\sqrt{3} \times \sqrt{3} \times 3$ phase (see Fig. S4(c) [51]). With $E_b = 6.30$ meV along TP$_1$, we obtain $R = 7.61 \times 10^{11}$ s^{-1} at 120 K above T_{CDW}, indicating strong CDW fluctuations among the degenerate configurations of the $\sqrt{3} \times \sqrt{3} \times 3$ phase with a characteristic lifetime of 0.91 ps [60]. Interestingly, this fluctuating CDW lifetime is comparable with that (~ 0.5 ps) measured by ultrafast spectroscopy in cuprates [62]. We note that such CDW fluctuations above T_{CDW} are similar to the case of CsV$_3$Sb$_5$ where the dynamic fluctuations of the $2 \times 2 \times 2$ CDW order was experimentally observed above $T_{CDW} = 94$ K up to ~ 160 K [39]. Just below T_{CDW}, the energy barrier from the $\sqrt{3} \times \sqrt{3} \times 3$ to the $\sqrt{3} \times \sqrt{3} \times 2$ phase is estimated as ~ 10.24 meV [see Figs. 3(a) and 3(d)], relatively higher than that (6.30 meV) along TP$_1$. Therefore, the long-range $\sqrt{3} \times \sqrt{3} \times 3$ phase can be kinetically trapped in certain temperature ranges below T_{CDW} without undergoing a transition to the $\sqrt{3} \times \sqrt{3} \times 2$ phase, which is supported by experimental evidence that the $\sqrt{3} \times \sqrt{3} \times 3$ phase was observed down to a temperature of ~ 50 K [32]. Furthermore, as shown in Fig. 4(b), a discontinuous change in ΔF with a sizable release of configurational entropy indicates the first-order character of CDW phase transition, consistent with the presence of a sharp peak in the measured specific heat data [32] at T_{CDW}. It is worth noting that, as T further decreases, both the energy barrier from the $\sqrt{3} \times \sqrt{3} \times 3$ to the $\sqrt{3} \times \sqrt{3} \times 2$ phase and its thermal activation rate are simultaneously lowered [see Fig. 3(a)]. Consequently, these two factors represent the compensation effect that determines whether the $\sqrt{3} \times \sqrt{3} \times 3$ phase remains kinetically trapped or is transformed into the $\sqrt{3} \times \sqrt{3} \times 2$ phase. Indeed, synchrotron x-ray diffraction experiments [40] observed the coexistence of the $\sqrt{3} \times \sqrt{3} \times 2$ and $\sqrt{3} \times \sqrt{3} \times 3$ charge correlations down to 15 K, indicating that the measured samples contain a mixture of short-range $\sqrt{3} \times \sqrt{3} \times 2$ and long-range $\sqrt{3} \times \sqrt{3} \times 3$ CDW orders at lower temperatures.

Discussion. Recently, IXS measurements [35] for ScV$_6$Sn$_6$ reported an unusual CDW formation process with two competing CDW instabilities: i.e., the long-range $\sqrt{3} \times \sqrt{3} \times 3$

CDW below T_{CDW} while the short-range $\sqrt{3} \times \sqrt{3} \times 2$ CDW above T_{CDW}. Across the CDW phase transition, the growth of an elastic central peak corresponding to the $\sqrt{3} \times \sqrt{3} \times 3$ CDW was observed together with phonon softening associated with the $\sqrt{3} \times \sqrt{3} \times 2$ CDW. It is, however, a puzzle that the soft phonon occurring at $q^* = (\frac{1}{3}, \frac{1}{3}, \frac{1}{2})$ is accompanied by the CDW formation at a different wavevector $q_s = (\frac{1}{3}, \frac{1}{3}, \frac{1}{3})$. Furthermore, the maximum IXS peak intensity of the $\sqrt{3} \times \sqrt{3} \times 3$ CDW is at least 3 orders of magnitude larger than that of the $\sqrt{3} \times \sqrt{3} \times 2$ CDW [35], implying that the former phase has significantly larger domain sizes in the measured samples than the latter one. Therefore, it is unlikely that there exists a first-order transformation from the short-range $\sqrt{3} \times \sqrt{3} \times 2$ to the long-range $\sqrt{3} \times \sqrt{3} \times 3$ CDW orders, driven by the scenario of a momentum-dependent electron-phonon coupling favoring q_s CDW as the ground state [35]. Instead, we believe that the observed first-order transition is of an order-disorder type between the static $\sqrt{3} \times \sqrt{3} \times 3$ CDW and its fluctuations, as discussed above. Here, the dynamic fluctuations of $\sqrt{3} \times \sqrt{3} \times 3$ CDW above T_{CDW} should sharply weaken the intensity of elastic central peak at q_s, as measured by IXS [35]. Meanwhile, according to synchrotron x-ray diffraction measurements [40], the short-ranged charge correlations of the $\sqrt{3} \times \sqrt{3} \times 2$ phase was observed in a wide range of temperatures between 15 and 300 K. This may be explained in terms of the local ordering character of the $\sqrt{3} \times \sqrt{3} \times 2$ phase due to a relatively higher energy barrier between its degenerate configurations [see Fig. 3(c)]. More refined experimental identifications of the phase-dependent CDW fluctuations above T_{CDW} are needed in the future.

In conclusion, based on first-principles calculations, we have demonstrated that the CDW order in ScV_6Sn_6 is driven by a Jahn-Teller-like effect involving the Sn1-Sn1 bond distortions, charge redistribution, and partial band-gap opening. Furthermore, our free-energy analysis revealed that the configurational entropy in the $\sqrt{3} \times \sqrt{3} \times 3$ phase emerges above T_{CDW} due to CDW fluctuations, while below T_{CDW}, the long-range $\sqrt{3} \times \sqrt{3} \times 3$ CDW order is kinetically trapped, indicating a first-order, order-disorder phase transition. Our findings clarify the driving mechanism of CDW and the order-disorder nature of CDW phase transition in ScV_6Sn_6, which have important implications for understanding the observed first-order transition with CDW fluctuations in other kagome metal compounds such as AV_3Sb_5 [37–39] and FeGe [63].

[1] L. Ye, M. Kang, J. Liu, F. von Cube, C. R. Wicker, T. Suzuki, C. Jozwiak, A. Bostwick, E. Rotenberg, D. C. Bell, L. Fu, R. Comin, and J. G. Checkelsky, Massive Dirac fermions in a ferromagnetic kagome metal, Nature (London) **555**, 638 (2018).

[2] Y.-P. Lin and R. M. Nandkishore, Complex charge density waves at Van Hove singularity on hexagonal lattices: Haldane-model phase diagram and potential realization in the kagome metals AV_3Sb_5 (A=K, Rb, Cs), Phys. Rev. B **104**, 045122 (2021).

[3] Z. Lin, C. Wang, P. Wang, S. Yi, L. Li, Q. Zhang, Y. Wang, Z. Wang, H. Huang, Y. Sun *et al.*, Dirac fermions in antiferromagnetic FeSn kagome lattices with combined space inversion and time-reversal symmetry, Phys. Rev. B **102**, 155103 (2020).

[4] S. Nakatsuji, N. Kiyohara, and T. Higo, Large anomalous Hall effect in a non-collinear antiferromagnet at room temperature, Nature (London) **527**, 212 (2015).

[5] A. K. Nayak, J. E. Fischer, Y. Sun, B. Yan, J. Karel, A. C. Komarek, C. Shekhar, N. Kumar, W. Schnelle, J. Kübler, C. Felser, and S. S. P. Parkin, Large anomalous Hall effect driven by a nonvanishing Berry curvature in the noncolinear antiferromagnet Mn_3Ge, Sci. Adv. **2**, e1501870 (2016).

[6] E. Liu, Y. Sun, N. Kumar, L. Muechler, A. Sun, L. Jiao, S.-Y. Yang, D. Liu, A. Liang, Q. Xu *et al.*, Giant anomalous Hall effect in a ferromagnetic kagome-lattice semimetal, Nat. Phys. **14**, 1125 (2018).

[7] L. Balents, Spin liquids in frustrated magnets, Nature (London) **464**, 199 (2010).

[8] S. Yan, D. A. Huse, and S. R. White, Spin-liquid ground state of the S = 1/2 Kagome Heisenberg antiferromagnet, Science **332**, 1173 (2011).

[9] Z. Lin, J.-H. Choi, Q. Zhang, W. Qin, S. Yi, P. Wang, L. Li, Y. Wang, H. Zhang, Z. Sun *et al.*, Flat bands and emergent ferromagnetic ordering in Fe_3Sn_2 kagome lattices, Phys. Rev. Lett. **121**, 096401 (2018).

[10] B. R. Ortiz, L. C. Gomes, J. R. Morey, M. Winiarski, M. Bordelon, J. S. Mangum, I. W. H. Oswald, J. A. Rodriguez-Rivera, J. R. Neilson, S. D. Wilson, E. Ertekin, T. M. McQueen, E. S. Toberer, New kagome prototype materials: Discovery of KV_3Sb_5, RbV_3Sb_5, and CsV_3Sb_5, Phys. Rev. Mater. **3**, 094407 (2019).

[11] Y.-X. Jiang, J.-X. Yin, M. M. Denner, N. Shumiya, B. R. Ortiz, J. He, X. Liu, S. S. Zhang, G. Chang, I. Belopolski *et al.*, Unconventional chiral charge order in kagome superconductor KV_3Sb_5, Nat. Mater. **20**, 1353 (2021).

[12] B. R. Ortiz, S. M. L. Teicher, Y. Hu, J. L. Zuo, P. M. Sarte, E. C. Schueller, A. M. Milinda Abeykoon, M. J. Krogstad, S. Rosenkranz, R. Osborn, R. Seshadri, L. Balents, J. He, and S. D. Wilson, CsV_3Sb_5: A Z2 topological kagome metal with a superconducting ground state, Phys. Rev. Lett. **125**, 247002 (2020).

[13] B. R. Ortiz, P. M. Sarte, E. M. Kenney, M. J. Graf, S. M. L. Teicher, R. Seshadri, and S. D. Wilson, Superconductivity in the Z2 kagome metal KV$_3$Sb$_5$, Phys. Rev. Mater. **5**, 034801 (2021).

[14] Q. Yin, Z. Tu, C. Gong, Y. Fu, S. Yan, and H. Lei, Superconductivity and normal-state properties of kagome metal RbV$_3$Sb$_5$ single crystals, Chin. Phys. Lett. **38**, 037403 (2021).

[15] S.-Y. Yang, Y. Wang, B. R. Ortiz, D. Liu, J. Gayles, E. Derunova, R. Gonzalez-Hernandez, L. Smejkal, Y. Chen, S. S. Parkin, S. D. Wilson, E. S. Toberer, T. McQueen, and M. N. Ali, Giant unconventional anomalous Hall effect in the metallic frustrated magnet candidate, Sci. Adv. **6**, eabb6003 (2020).

[16] F. H. Yu, T. Wu, Z. Y. Wang, B. Lei, W. Z. Zhuo, J. J. Ying, and X. H. Chen, Concurrence of anomalous Hall effect and charge density wave in a superconducting topological kagome metal, Phys. Rev. B **104**, L041103 (2021).

[17] L. Nie, K. Sun, W. Ma, D. Song, L. Zheng, Z. Liang, P. Wu, F. Yu, J. Li, M. Shan et al., Concurrence of anomalous Hall effect and charge density wave in a superconducting topological kagome metal, Nature (London) **604**, 59 (2022).

[18] Z. Jiang, H. Ma, W. Xia, Z. Liu, Q. Xiao, Z. Liu, Y. Yang, J. Ding, Z. Huang, J. Liu et al., Observation of electronic nematicity driven by the three-dimensional charge density wave in Kagome lattice KV$_3$Sb$_5$, Nano Lett. **23**, 5625 (2023).

[19] F. H. Yu, D. H. Ma, W. Z. Zhuo, S. Q. Liu, X. K. Wen, B. Lei, J. J. Ying, and X. H. Chen, Unusual competition of superconductivity and charge-density-wave state in a compressed topological kagome metal, Nat. Commun. **12**, 3645 (2021).

[20] K. Y. Chen, N. N. Wang, Q. W. Yin, Y. H. Gu, K. Jiang, Z. J. Tu, C. S. Gong, Y. Uwatoko, J. P. Sun, H. C. Lei, J. P. Hu, and J.-G. Cheng, Double superconducting dome and triple enhancement of T_c in the kagome superconductor CsV$_3$Sb$_5$ under high pressure, Phys. Rev. Lett. **126**, 247001 (2021).

[21] Z. Zhang, Z. Chen, Y. Zhou, Y. Yuan, S. Wang, J. Wang, H. Yang, C. An, L. Zhang, X. Zhu, Y. Zhou, X. Chen, J. Zhou, and Z. Yang, Pressure-induced reemergence of superconductivity in the topological kagome metal CsV$_3$Sb$_5$, Phys. Rev. B **103**, 224513 (2021).

[22] C. Wang, S. Liu, H. Jeon, Y. Jia, and J.-H. Cho, Charge density wave and superconductivity in the kagome metal CsV$_3$Sb$_5$ around a pressure-induced quantum critical point, Phys. Rev. Mater. **6**, 094801 (2022).

[23] R. E. Peierls, Quantum Theory of Solids (Oxford University Press, New York, 1955).

[24] W. Kohn, Image of the fermi surface in the vibration spectrum of a metal, Phys. Rev. Lett. **2**, 393 (1959).

[25] M. L. Kiesel, C. Platt, and R. Thomale, Unconventional fermi surface instabilities in the kagome Hubbard model, Phys. Rev. Lett. **110**, 126405 (2013).

[26] W.-S. Wang, Z.-Z. Li, Y.-Y. Xiang, and Q.-H. Wang, Competing electronic orders on kagome lattices at van Hove filling, Phys. Rev. B **87**, 115135 (2013).

[27] H. Luo, Q. Gao, H. Liu, Y. Gu, D. Wu, C. Yi, J. Jia, S. Wu, X. Luo, Y. Xu, L. Zhao, Q. Wang, H. Mao, G. Liu, Z. Zhu, Y. Shi, K. Jiang, J. Hu, Z. Xu, and X. J. Zhou, Electronic nature of charge density wave and electron-phonon coupling in Kagome superconductor KV$_3$Sb$_5$, Nat. Commun. **13**, 273 (2022).

[28] S. Cho, H. Ma, W. Xia, Y. Yang, Z. Liu, Z. Huang, Z. Jiang, X. Lu, J. Liu, Z. Liu et al., Emergence of new van hove singularities in the charge density wave state of a topological kagome metal RbV$_3$Sb$_5$, Phys. Rev. Lett. **127**, 236401 (2021).

[29] Z. Wang, S. Ma, Y. Zhang, H. Yang, Z. Zhao, Y. Ou, Y. Zhu, S. Ni, Z. Lu, H. Chen et al., Distinctive momentum dependent charge-density-wave gap observed in CsV$_3$Sb$_5$ superconductor with topological Kagome lattice, arXiv:2104.05556.

[30] K. Nakayama, Y. Li, T. Kato, M. Liu, Z. Wang, T. Takahashi, Y. Yao, and T. Sato, Multiple energy scales and anisotropic energy gap in the charge-density-wave phase of Kagome superconductor CsV$_3$Sb$_5$, Phys. Rev. B **104**, L161112 (2021).

[31] G. Liu, X. Ma, K. He, Q. Li, H. Tan, Y. Liu, J. Xu, W. Tang, K. Watanabe, T. Taniguchi, L. Gao, Y. Dai, H.-H. Wen, B. Yan, and X. Xi, Observation of anomalous amplitude modes in the kagome metal CsV$_3$Sb$_5$, Nat. Commun. **13**, 3461 (2022).

[32] H. W. S. Arachchige, W. R. Meier, M. Marshall, T. Matsuoka, R. Xue, M. A. McGuire, R. P. Hermann, H. Cao, and D. Mandrus, Charge density wave in kagome lattice intermetallic ScV$_6$Sn$_6$, Phys. Rev. Lett. **129**, 216402 (2022).

[33] C. Wang, S. Liu, H. Jeon, and J.-H. Cho, Origin of charge density wave in the layered kagome metal CsV$_3$Sb$_5$, Phys. Rev. B **105**, 045135 (2022).

[34] H. Tan and B. Yan, Abundant lattice instability in kagome metal ScV$_6$Sn$_6$, Phys. Rev. Lett. **130**, 266402 (2023).

[35] S. Cao, C. Xu, H. Fukui, T. Manjo, Y. Dong, M. Shi, Y. Liu, C. Cao, and Y. Song, Competing charge-density wave instabilities in the kagome metal ScV$_6$Sn$_6$, Nat. Commun. **14**, 7671 (2023).

[36] A. Korshunov, H. Hu, D. Subires, Y. Jiang, D. Călugăru, X. Feng, A. Rajapitamahuni, C. Yi, S. Roychowdhury, M. G. Vergniory, J. Strempfer, C. Shekhar, E. Vescovo, D. Chernyshov, A. H. Said, A. Bosak, C. Felser, B. Andrei Bernevig, and S. Blanco-Canosa, Softening of a flat phonon mode in the kagome ScV$_6$Sn$_6$, Nat. Commun. **14**, 6646 (2023).

[37] D. Subires, A. Korshunov, A. H. Said, L. Sãnchez, B. R. Ortiz, S. D. Wilson, A. Bosak, and S. Blanco-Canosa, Order-disorder charge density wave instability in the kagome metal (Cs, Rb)V$_3$Sb$_5$, Nat. Commun. **14**, 1015 (2023).

[38] K. Yang, W. Xia, X. Mi, L. Zhang, Y. Gan, A. Wang, Y. Chai, X. Zhou, X. Yang, Y. Guo, and M. He, Charge fluctuations above TCDW revealed by glass like thermal transport in kagome metals AV$_3$Sb$_5$ (A=K, Rb, Cs), Phys. Rev. B **107**, 184506 (2023).

[39] Q. Chen, D. Chen, W. Schnelle, C. Felser, and B. D. Gaulin, Charge density wave order and fluctuations above T_{CDW} and below superconducting T_c in the kagome metal CsV$_3$Sb$_5$, Phys. Rev. Lett. **129**, 056401 (2022).

[40] G. Pokharel, B. R. Ortiz, L. Kautzsch, S. J. Gomez Alvarado, K. Mallayya, G. Wu, E.-A. Kim, J. P. C. Ruff, S. Sarker, and S. D. Wilson, Frustrated charge order and cooperative distortions in ScV$_6$Sn$_6$, Phys. Rev. Mater. **7**, 104201 (2023).

[41] Our first-principles DFT calculations were performed using the Vienna ab initio simulation package with the projector-augmented wave method [42–44]. For the exchange-correlation energy, we employed the generalized-gradient approximation functional of Perdew-Burke-Ernzerhof [45]. The plane wave basis was employed with a kinetic energy cutoff of 400 eV, and the k-space integration was done with $12 \times 12 \times 8$, $6 \times 6 \times 4$, and $8 \times 8 \times 8$ meshes for the pristine, $\sqrt{3} \times \sqrt{3} \times 2$, and $\sqrt{3} \times \sqrt{3} \times 3$ phases, respectively. Here, the $\sqrt{3} \times \sqrt{3} \times 2$ and $\sqrt{3} \times \sqrt{3} \times 3$ structures were considered with the hexagonal and primitive rhombohedral unit cells, respectively [see Fig. 1(b)]. All atoms were allowed to relax along the calculated forces until all the residual force components were less than 0.001 eV/Å. The unfolded electronic band structure was calculated

using the Vaspkit software [46]. The phonon dispersions were calculated using the finite displacement method implemented in the phonopy software [47,48]. To calculate an energy barrier along the transition pathway between the $\sqrt{3} \times \sqrt{3} \times 2$ and $\sqrt{3} \times \sqrt{3} \times 3$ phases, we used the nudged elastic band method [49,50] within the same $\sqrt{3} \times \sqrt{3} \times 6$ supercell.

[42] G. Kresse and J. Hafner, *Ab initio* molecular dynamics for open-shell transition metals, Phys. Rev. B **48**, 13115 (1993).

[43] G. Kresse and J. Furthmüller, Efficiency of *ab-initio* total energy calculations for metals and semiconductors using a plane-wave basis set, Comput. Mater. Sci. **6**, 15 (1996).

[44] P. E. Blöchl, Projector augmented-wave method, Phys. Rev. B **50**, 17953 (1994).

[45] J. P. Perdew, K. Burke, and M. Ernzerhof, Generalized gradient approximation made simple, Phys. Rev. Lett. **77**, 3865 (1996); **78**, 1396(E) (1997).

[46] V. Wang, N. Xu, J.-C. Liu, G. Tang, and W.-T. Geng, VASPKIT: A user-friendly interface facilitating high-throughput computing and analysis using VASP code, Comput. Phys. Commun. **267**, 108033 (2021).

[47] A. Togo, L. Chaput, T. Tadano, and I. Tanaka, Implementation strategies in phonopy and phono3py, J. Phys. Soc. Jpn. **92**, 012001 (2023).

[48] A. Togo and I. Tanaka, First principles phonon calculations in materials science, Scr. Mater. **108**, 1 (2015).

[49] G. Henkelman, B. P. Uberuaga, H. Jónsson, A climbing image nudged elastic band method for finding saddle points and minimum energy paths, J. Chem. Phys. **113**, 9901 (2000).

[50] D. Sheppard, P. Xiao, W. Chemelewski, D. D. Johnson, and G. Henkelman, A generalized solid-state nudged elastic band method, J. Chem. Phys. **136**, 074103 (2012).

[51] See Supplemental Material at http://link.aps.org/supplemental/10.1103/PhysRevB.109.L121103 for the band projections onto the V and Sn orbitals, the phonon spectrum of the pristine and $\sqrt{3} \times \sqrt{3} \times 3$ phases, the unfolded band structures of the pristine, $\sqrt{3} \times \sqrt{3} \times 2$, and $\sqrt{3} \times \sqrt{3} \times 3$ phases, the variation of $T\Delta S$ and ΔE_{vib} as a function of T, the total DOS of the $\sqrt{3} \times \sqrt{3} \times 2$ and $\sqrt{3} \times \sqrt{3} \times 3$ phases, and the degenerate configurations of the $\sqrt{3} \times \sqrt{3} \times 3$ phase.

[52] A combined study of angle-resolved photoemission spectroscopy (ARPES) and DFT of ScV_6Sn_6 [53] showed that the DFT band structures of the saddle points originating from the V $3d$ orbitals are consistent with the ARPES data. Recent optical reflection measurements of ScV_6Sn_6 [54] also reported that the interband transitions associated with the saddle points at the M point are hardly affected across the CDW transition and that the observed and DFT-predicted optical conductivities are in good agreement with each other. Since the previous and present DFT band structures are nearly the same (see Fig. S2 [51]), we can say that our DFT calculations properly capture the single-particle excitation spectra measured by ARPES [53] and infrared spectroscopy [54].

[53] S. Lee, C. Won, J. Kim, J. Yoo, S. Park, J. Denlinger, C. Jozwiak, A. Bostwick, E. Rotenberg, R. Comin, M. Kang, and

J.-H. Park, Nature of charge density wave in kagome metal ScV_6Sn_6, arXiv:2304.11820.

[54] T. Hu, H. Pi, S. Xu, L. Yue, Q. Wu, Q. Liu, S. Zhang, R. Li, X. Zhou, J. Yuan *et al.*, Optical spectroscopy and band structure calculations of the structural phase transition in the vanadium-based kagome metal ScV_6Sn_6, Phys. Rev. B **107**, 165119 (2023).

[55] Since the DFT band structures of ScV_6Sn_6 agree well with the ARPES [53] and infrared spectroscopy [54] data [52], we can calculate the low-frequency limit of the imaginary part of electronic susceptibility from the DFT band dispersion, defined as $\text{Im}[\chi_0(q)] = \sum_{nm} \int d\mathbf{k} \delta(\varepsilon_{n\mathbf{k}} - E_F)\delta(\varepsilon_{m\mathbf{k}+\mathbf{q}} - E_F)$. As shown in Fig. S3 [51], the calculated $\text{Im}[\chi_0(q)]$ curves for ScV_6Sn_6 and YV_6Sn_6 exhibit similar patterns with no dominant peaks at the CDW wavevectors $H = (\frac{1}{3}, \frac{1}{3}, \frac{1}{2})$ and $\overline{K} = (\frac{1}{3}, \frac{1}{3}, \frac{1}{3})$ for the $\sqrt{3} \times \sqrt{3} \times 2$ and $\sqrt{3} \times \sqrt{3} \times 3$ phases, respectively. Here, the results for ScV_6Sn_6 are in good agreement with previous DFT calculations [34,54]. Despite similar band structures [see Figs. S2(b) and S2(c)] and electronic susceptibilities of ScV_6Sn_6 and YV_6Sn_6, only ScV_6Sn_6 exhibits a CDW instability, indicating that electron-electron interactions are unlikely the dominant driving force of the CDW formation in ScV_6Sn_6.

[56] W. R. Meier, R. P. Madhogaria, S. Mozaffari, M. Marshall, D. E. Graf, M. A. McGuire, H. W. S. Arachchige, C. L. Allen, J. Driver, H. Cao, and D. Mandrus, Tiny Sc allows the chains to rattle: impact of Lu and Y doping on the charge-density wave in ScV_6Sn_6, J. Am. Chem. Soc. **145**, 20943 (2023).

[57] S. Cheng, Z. Ren, H. Li, J. Oh, H. Tan, G. Pokharel, J. M. DeStefano, E. Rosenberg, Y. Guo, Y. Zhang *et al.*, Nanoscale visualization and spectral fingerprints of the charge order in ScV_6Sn_6 distinct from other kagome metals, npj Quantum Mater **9**, 14 (2024).

[58] The vibration energy is given by $E_{\text{vib}} = \sum_{\mathbf{q}N} \hbar\omega_{\mathbf{q}N}[\frac{1}{2} + \frac{1}{\exp(\hbar\omega_{\mathbf{q}N}/k_BT)-1}]$ where $\mathbf{q}$ and N represent the wave vector and band index of phonon modes, respectively. The calculated result of $\Delta E_{\text{vib}}(T)$ is displayed in Fig. S6 [51].

[59] S. Arrhenius, Über die Reaktionsgeschwindigkeit bei der Inversion von Rohrzucker durch Säuren, Z. Phys. Chem. **4U**, 226 (1889).

[60] The characteristic lifetime (half lifetime) of the transition between two degenerate $\sqrt{3} \times \sqrt{3} \times 3$ configurations is calculated using the equation $t_{1/2} = \ln(2)/R$ [61].

[61] J. I. Steinfeld, J. S. Francisco, and W. L. Hase, *Chemical Kinetics and Dynamics*, 2nd ed. (Prentice Hall, NJ, 1999).

[62] D. H. Torchinsky, F. Mahmood, A. T. Bollinger, I. Bozovic, and N. Gedik, Fluctuating charge-density waves in a cuprate superconductor, Nat. Mater. **12**, 387 (2013).

[63] C. Shi, Y. Liu, B. B. Maity, Q. Wang, S. R. Kotla, S. Ramakrishnan, C. Eisele, H. Agarwal, L. Noohinejad, Q. Tao, B. Kang, Z. Lou, X. Yang, Y. Qi, X. Lin, Z. Xu, A. Thamizhavel, G. Cao, S. V. Smaalen, S. Cao *et al.*, Disordered structure for long-range charge density wave order in annealed crystals of magnetic kagome FeGe, arXiv:2308.09034.